Scripta Materialia 188 (2020) 107–111

Contents lists available at ScienceDirect

Scripta Materialia

journal homepage: www.elsevier.com/locate/scriptamat

Room-temperature NO_2 sensor based on a hybrid nanomaterial of methylammonium tin iodide submicron spheres and tin dioxide nanowires

Vu Xuan Hien[a], Phung Dinh Hoat[c], Pham Tien Hung[b,c], Sangwook Lee[c,d], Joon-Hyung Lee[c,d,*], Young-Woo Heo[c,d,*]

[a] School of Engineering Physics, Hanoi University of Science and Technology (HUST), No. 1 Dai Co Viet Street, Hanoi, Viet Nam
[b] School of Physics, Le Quy Don Technical University, Cau Giay District, Hanoi, Viet Nam
[c] School of Materials Science and Engineering, Kyungpook National University (KNU), E8-215, 80 Daehakro, Buk-gu, Daegu 702-701, Republic of Korea
[d] KNU Advanced Material Research Institute, Kyungpook National University, Daegu 41566, Republic of Korea

ARTICLE INFO

Article history:
Received 22 April 2020
Revised 5 July 2020
Accepted 12 July 2020

Keywords:
Halide perovskite
Lead free
Hybrid material
CVD
Gas sensor

ABSTRACT

Perovskite halide materials are currently attracting considerable attention owing to their superior optical and electrical properties. This study proposes a reliable process for synthesizing hybrid nanomaterials made of methylammonium tin iodide ($MASnI_3$) submicron spheres and tin dioxide (SnO_2) nanowires. Post-fabricated hybrid nanomaterials were investigated for NO_2 sensing properties at 25 °C in the dark. The effect of moisture on the NO_2 sensitivity of this material was investigated. The durability of sensor components using this material was also investigated. In this paper, we also discuss the NO_2 sensitivity mechanism of $MASnI_3/SnO_2$ hybrid nanomaterials in detail.

Along with the development of nanomaterials, hybrid materials are currently a high-potential research direction. Hybrid nanomaterials are formed by two or more different components connected on the nanometer scale. This type of material has properties that change according to the composition and morphology of the constituent materials [1]. Numerous studies show that hybrid nanomaterials exhibit special advantages in fields, such as optics, photovoltaics, fuel cells, catalysts, and sensors [2–8]. Hybrid nanomaterials are currently attracting considerable attention from research groups in the field of gas sensors [9–14].

Nitrous oxide (NO_2) is a very toxic gas that is often found in large industrial and urban areas. In the atmosphere, NO_2 and CO_2 are some causes of air pollution. NO_2 can seriously affect human health [15,16]. Specifically, a healthy person exposed to 300–800 ppb of NO_2 for less than 1 h can reduce lung capacity by 10% [17]. Therefore, the ppb-level detection of this gas leaked into the environment is an important issue. According to studies of semiconductor gas sensors, oxides and tin compounds are often highly sensitive to NO_2 [18–20]. Therefore, research on manufacturing and NO_2 gas-sensitive properties of Sn compound hybrid nanomaterials is developing [21,22].

Halide perovskites are advanced materials that have excellent optical and electrical properties [23,24]. This is a material that can be used in future optical detectors and solar cells [25,26]. Interestingly, many studies have shown that halide perovskites have very large resistance changes when exposed to reducing or oxidizing gases [27–30]. In 2018, Fu et al. found that $CH_3NH_3PbI_3$ is able to quickly detect 1 ppm of NO_2 at room temperature [31]. Recently, our team discovered that $MASnI_3$ membranes can detect NO_2 at ppb concentrations at 25 °C [20]. However, perovskite halide materials have a major disadvantage of being unstable in oxygen and light environments [32–34]. Y. Chen et al. showed that hybrid nanomaterials between SnO_2 and $MASnI_3$ nanoparticles can detect NO_2 at ppb concentrations with ultraviolet illumination [35]. Moreover, this hybrid material is capable of stable operation for at least 30 days. In this paper, we introduce a reliable process for making hybrid nanomaterials between SnO_2 nanowires and $MASnI_3$ submicron spheres via thermal evaporation. The NO_2 gas-sensitive properties of this hybrid nanomaterial were investigated and compared with those of other studies.

The process of manufacturing hybrid $MASnI_3/SnO_2$ materials involves two main stages: growth of SnO_2 nanowires and then synthesis of $MASnI_3$ submicron spheres onto the SnO_2 nanowires. For

* Corresponding authors at: School of Materials Science and Engineering, Kyungpook National University (KNU), E8-215, 80 Daehakro, Buk-gu, Daegu 702-701, Republic of Korea.
E-mail address: ywheo@knu.ac.kr (Y.-W. Heo).

https://doi.org/10.1016/j.scriptamat.2020.07.022
1359-6462/

the first stage, SiO_2/Si substrate are cleaned with trichlorethylene (TCE), acetone, and ethanol in an ultrasonic bath sequentially for 5 min. Gold nanoparticles were coated on the substrate for 10 s using a mini plasma sputtering coater (TCH-GSL-1100X-SPC12-LD). The substrate was then heated at 400 °C for 1 h using a horizontal furnace. After calcination, the gold film on the SiO_2 substrate became gold nanoparticles. The size and distribution of the gold nanoparticles are shown in Fig. S1 (see Supplementary document). To grow SnO_2 nanowires, 2 g of SnO powder (Sigma-Aldrich, powder particle size: ≤60 μm, 97%) were added to an alumina boat. The substrate coated with gold nanoparticles was placed on the boat in the opposite direction to the SnO powder (distance between the SnO powder and substrate was 8 mm). This alumina boat was fixed in a horizontal furnace at a pressure of 10^{-2} Torr. The growth of the SnO_2 wire was performed at 800 °C (heating rate of 5 °C/min) for 60 min. After the heat treatment process finished, the furnace was naturally cooled to room temperature.

$MASnI_3$ submicron spheres were synthesized on the SnO_2 nanowires by thermal evaporation using the setup diagram shown in Fig. S2 (see Supplementary document). Here, 1.0 g of SnO powder and 0.3 g of methylammonium iodide (MAI; Sigma-Aldrich, powder, 98%) were used as precursors. The SnO, MAI powder, and substrate with SnO_2 nanowires were fixed at different positions in the horizontal furnace so that their temperatures were 800 °C, 230 °C, and 120 °C, respectively. During $MASnI_3$ synthesis, 10 sccm of N_2 was injected into a quartz tube maintained at 5×10^{-3} Torr. The $MASnI_3$ phase on SnO_2 formed within 60 min. After the synthesis process completed, the furnace was naturally cooled to 100 °C. The sample was then quickly transferred into a glove box for storage.

The structure and surface morphology of the post-fabricated materials were characterized by X-ray diffraction (XRD; Xpert-Pro) using CuKα radiation ($\lambda = 1.5418$ Å) and field-emission scanning electron microscopy (FE-SEM; JEOL JSM-7610F). Additionally, the structure and elemental mapping of this hybrid material were investigated in detail by transmission electron microscopy (TEM; Telnai G2F20 S-TWIN, Philips) combined with energy-dispersive X-ray spectroscopy (EDX). To investigate the gas sensing properties of the as-synthesized material, a gold interdigitated electrode was evaporated onto the surface of the sample by thermal evaporation. The structure of the material after coating the interdigitated electrode is shown in Fig. S3 (see Supplementary document). The gas sensing properties of the material were studied by an aerodynamic measuring system. The structure and design of the measuring system are described in Fig. S4 (see Supplementary document). Measurements were performed in the dark with a carrier gas of dry air (total flow rate of 300 sccm). The chemical composition of the $MASnI_3/SnO_2$ hybrid was detected by X-ray photoelectron spectroscopy (XPS; Quantera SXM). In this characterization, the binding energy data was calibrated using C 1s peak at 284.6 eV.

The structures and surface morphologies of the materials are summarized in Fig. 1. Here, the major peaks at 2θ of 26.6°, 33.9°, and 51.8° are consistent with the corresponding diffraction planes of (110), (011), and (121) of tetragonal-structured SnO_2 [ICSD; Ref. code: 98-016-9033]. The FE-SEM image in Fig. 1(b) shows that the fabricated SnO_2 nanowires have a density of appearance and length that was greater than 5 μm. After growing the $MASnI_3$ submicron spheres on the SnO_2 nanowires, the remaining diffraction peaks were consistent with those corresponding to the cubic structure of $MASnI_3$ [ICOD: PDF-2; Ref. code: 00-032-1928]. In this XRD result, no strange peaks for other materials appeared, which confirmed the high purity of the fabricated material. The XPS analysis of the sample in Fig. S5 (Supplementary document) confirm the existence of $CH_3NH_3SnI_3$ in which the binding energy of the Sn $3d_{3/2}$, Sn $3d_{5/2}$, I $3d_{3/2}$, and I $3d_{5/2}$ peaks are 492.9 eV, 484.5 eV, 628.4 eV, and 616.9 eV, respectively [36]. The surface morphology of this material is shown in Fig. 1(c). Along with the elemental mapping images in Fig. S6 (Supplementary document), $MASnI_3$ submicron spheres with an average diameter of 200 nm are grown along the SnO_2 nanowires. In addition, the $MASnI_3$ submicron spheres are in good contact with the SnO_2 nanowires.

The morphologies and crystal structures of the as-fabricated hybrid $MASnI_3/SnO_2$ nanomaterials were further investigated by TEM, HR-TEM, and SEAD, as shown in Fig. 2. Based on the images in Fig. 2 (a–c), the SnO_2 nanowire had a diameter of approximately 20 nm, and the $MASnI_3$ material growing along this wire had a diameter consistent with the results obtained on the FE-SEM image (Fig. 1). The HR-TEM image in Fig. 2(e) indicates that the SnO_2 nanowire has a single crystal structure with a measured distance between crystal faces of 3.3 nm (inset image in Fig. 2(d)) corresponding to the distance between the (110) faces of SnO_2. Meanwhile, the $MASnI_3$ material was in polycrystalline form with a distance between the crystal faces calculated at some locations to be 3.1 nm (inset image in Fig. 2(f)) corresponding to the distance between (200) faces of $MASnI_3$. These assertions were verified by the SEAD patterns of the SnO_2 nanowire and submicron $MASnI_3$ spheres, as shown in Fig. 2(d) and (e), respectively.

The gas sensing measurement results are shown in Fig. 3. Fig. 3a showing that the resistance of the SnO_2 nanowire remained almost unchanged when 1 ppm NO_2 was present. In contrast, the hybrid material between the SnO_2 nanowire and $MASnI_3$ submicron spheres could change resistance when there was 1 ppm of NO_2 at 25 °C in the dark. Because SnO_2 nanowires are not sensitive to NO_2 at 25 °C in the dark, the NO_2-sensing ability of this hybrid material likely originates from the $MASnI_3$ submicron spheres. This is reasonable because our previous study showed that $MASnI_3$ membranes are sensitive to NO_2 at 25 °C in the dark [20]. However, we encountered an issue when investigating the gas sensing properties of the $MASnI_3$ membrane because its resistance is too large (~ GΩ at 25 °C). This has also been the case in other studies on the gas sensing characteristics of halide perovskites [31,37]. By hybridizing the $MASnI_3$ material with SnO_2 material, the resistance of this material system was reduced to ~25 kΩ at 25 °C, which is even smaller than that of the SnO_2 nanowire. This seems to have very little association with the p–n transition of $MASnI_3$ and SnO_2, as presented by the study by Chen et al. [35]. In our case, many $MASnI_3$ submicron spheres along the SnO_2 nanowire correspond to the model of multiple large resistors in parallel with one small resistor. As a result, the resistance of this material system will be less than the minimum value of the system resistance. Fig. 3b shows a comparison of the gas sensitivity of $MASnI_3/SnO_2$ hybrid materials to different gases at 25 °C. This hybrid material is only sensitive to NO_2 gas under the same survey conditions. The stability and durability of $MASnI_3/SnO_2$ hybrid materials under NO_2 conditions and humidity are shown in Fig. 3 (cand d). According to the results shown in Fig. 3(c), the resistance of this material increased and decreased steadily after five pulses of NO_2. Without humidity, this hybrid nanomaterial was found to be capable of stable operation for at least 30 working days. When moisture was present in the chamber, the durability of this material reduced to 20 and 10 days, respectively, at humidities of 50% and 90% (Fig. 3(d)). Afterwards, the responsiveness of this hybrid material tended to decrease. The influence of NO_2 concentration on the sensor response was also investigated, as shown in Fig. 3(e). The smallest concentration of NO_2 that this hybrid material could detect was 25 ppb with a response of approximately 10. The fitting line for this data is shown in Fig. 3(f) with a coefficient of determination (R^2) of 99.7%. The effects of different carrier gas (dry air versus oxygen) on the NO_2 response of the sample can be found in Fig. S7 (Supplementary document). For $MASnI_3$ material, a decline in the NO_2 response when using O_2 as a carrier gas was explained in detail in our pre-

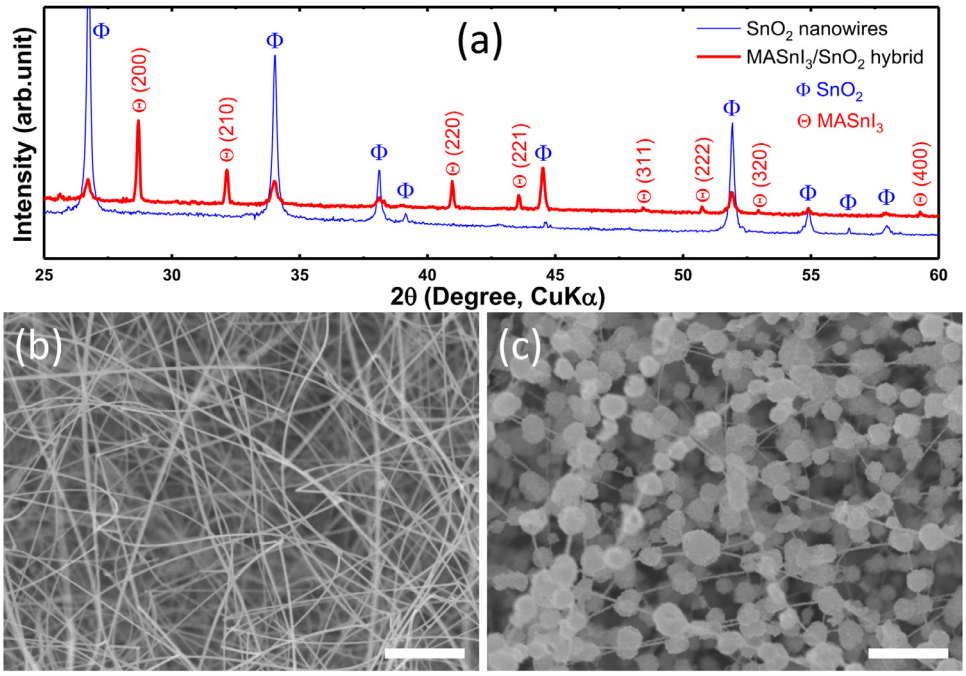

Fig. 1. XRD patterns (a) and FE-SEM images of the as-synthesized SnO_2 nanowires (b) and $MaSnI_3/SnO_2$ hybrid (c). The scale bar is 1 μm.

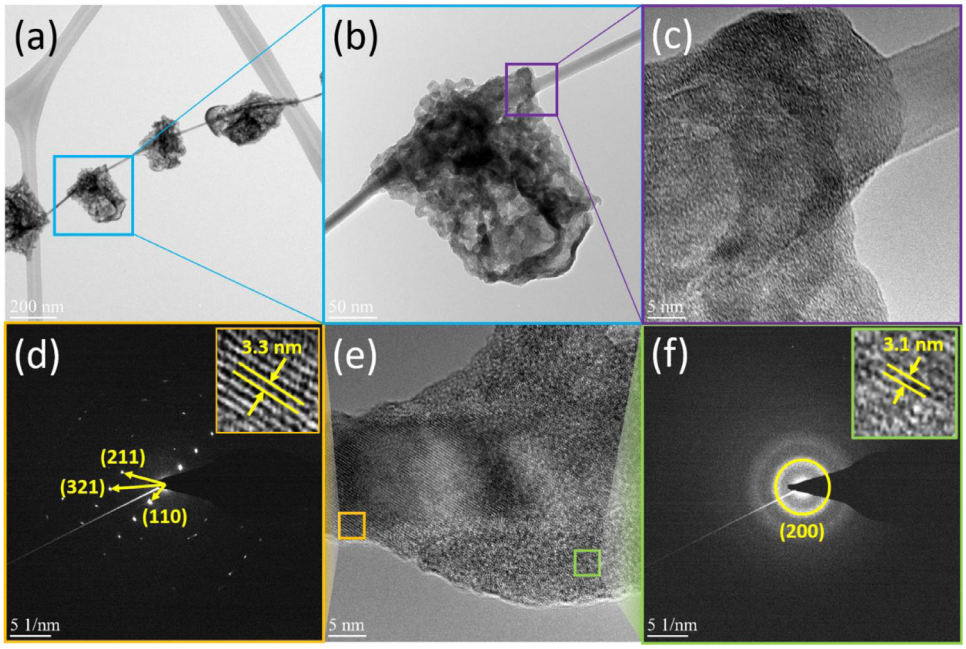

Fig. 2. TEM images (a, b), HR-TEM images (c, e) and SEAD patterns (d, f) of the $MASnI_3/SnO_2$ hybrid. The inset images show magnified HR-TEM images at the corresponding marked locations in Figure (e).

vious study [20]. With the carrier gas of oxygen, the $MASnI_3/SnO_2$ hybrid is still selective toward NO_2.

$MASnI_3$ material is known as a p-type semiconductor; thus, the resistance of this material will normally decrease when exposed to oxidizing gases, such as NO_2 [20,31]. However, hybrid nanomaterials between $MASnI_3$ and SnO_2 have an increased resistance when exposed to NO_2. This can be explained by our proposed model shown in Fig. 4. In this model, a $MASnI_3$ submicron sphere is attached to a SnO_2 wire, as shown by the FE-SEM (Fig. 1) and TEM (Fig. 2) images. Because SnO_2 nanowire materials do not respond to NO_2 at 25 °C in the dark, the sensitive material in this hybrid is $MASnI_3$. However, the SnO_2 nanowire will serve as the connection material between the electrodes. Typically, physisorption and chemisorption of oxygen molecules on the surface of a p-type semiconductor results in an accumulation zone (dark brown area) near the surface of the material [38]. This accumulation area may concentrate many carriers of p-type semiconductors, which are holes. With a p–n transition, a p-type material is known as an electron suction material at the region adjacent to the n-type material [39–41]. According to this mechanism, a depletion zone is formed on the SnO_2 side. Like O_2, NO_2 may be physically and chemically adsorbed onto the $MASnI_3$ surface via the following re-

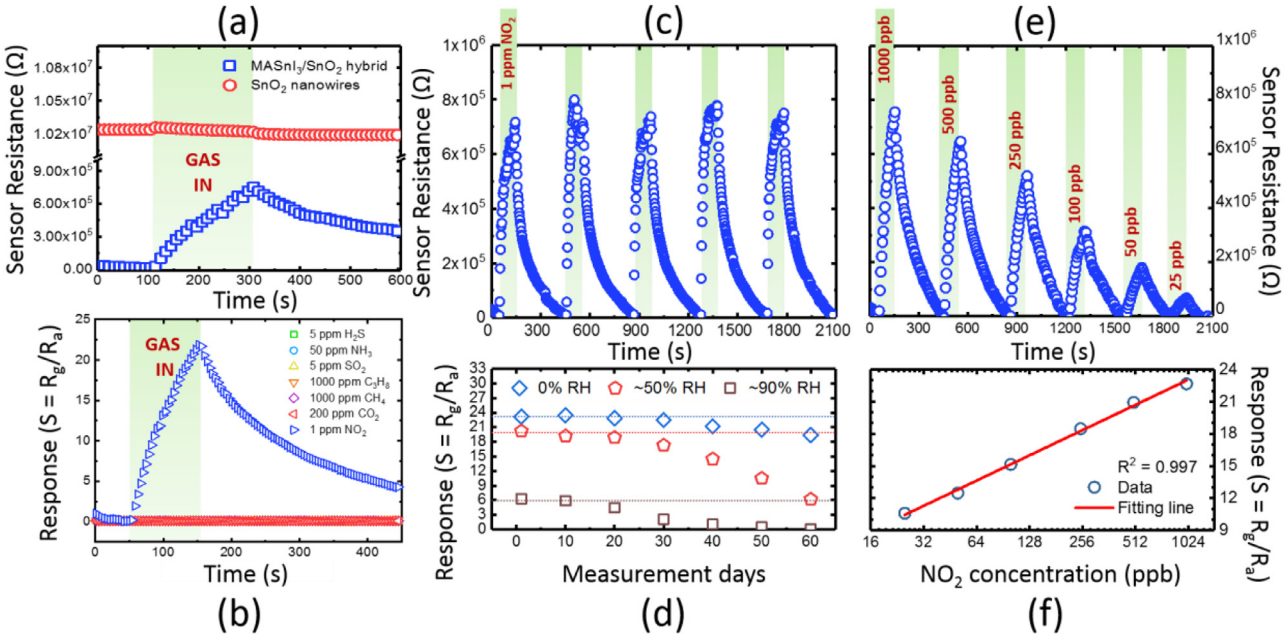

Fig. 3. Response and recovery curves of the SnO_2 nanowires versus the $MASnI_3/SnO_2$ hybrid (a). Comparison of the responsiveness of the $MASnI_3/SnO_2$ hybrid nanomaterials to several gases (b). Modulation curve of the $MASnI_3/SnO_2$ hybrid toward 1 ppm of NO_2 (c). $MASnI_3/SnO_2$ hybrid material response within 60 working days under the influence of moisture (d). $MASnI_3/SnO_2$ hybrid response/recovery curve with NO_2 concentrations of 25–1000 ppb (e) and the fitting line (f).

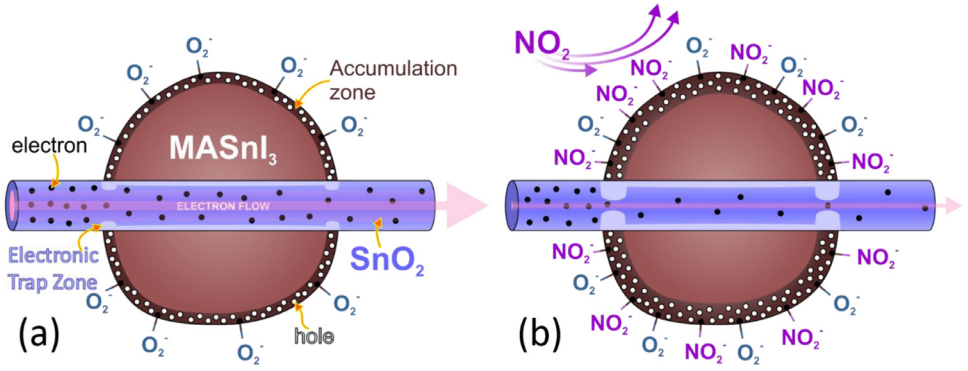

Fig. 4. Gas-sensitive model of the $MASnI_3/SnO_2$ hybrid material before (a) and after (b) the injection of NO_2 gas.

action:

$$NO_2(g) \rightarrow NO_2^- + h^+ \quad (1)$$

Moreover, NO_2 can react with adsorbed oxygen ions (in the model, O_2^-) as follows:

$$NO_2(g) + O_2^-(ads) \rightarrow NO_2^-(ads) + 2O^-(ads) + h^+ \quad (2)$$

$$NO_2(g) + 2O^-(ads) \rightarrow NO_2^-(ads) + O^{2-}(ads) + 2h^+ \quad (3)$$

These reactions may widen the accumulation zone by an increase in the entire concentration in the p-type $MASnI_3$. Therefore, the electron channel of the SnO_2 narrowed with the widened depletion region owing to the adsorption of NO_2 on the $MASnI_3$ surface, which resulted in the resistance increase of the hybrid.

In conclusion, a hybrid nanomaterial consisting of $MASnI_3$ submicron spheres and SnO_2 nanowires was synthesized in two steps of thermal evaporation. This hybrid nanomaterial is high purity with a SnO_2 nanowire diameter and $MASnI_3$ spherical diameter of 20 and 200 nm, respectively. The NO_2 sensitivity of these $MASnI_3/SnO_2$ hybrid nanomaterials was found to be considerably superior to that of SnO_2 nanowires. Additionally, the hybridization of $MASnI_3$ with SnO_2 reduced the resistance to kΩ levels, in contrast to the GΩ levels for $MASnI_3$ films. Thus, this nanomaterial can be easily integrated with electronic circuits in applications. This hybrid nanomaterial is almost selective for NO_2 at 25 °C in the dark. With a humidity of less than 50%, this material is capable of stable operation for 30 days. The smallest NO_2 concentration that this hybrid material can detect is 25 ppb with a response of 10. Additionally, a NO_2 sensitivity mechanism of this hybrid nanomaterial has been proposed and discussed.

Declaration of Competing Interest

The authors declare that they have no known competing financial interests or personal relationships that could have appeared to influence the work reported in this paper.

Acknowledgments

This work was supported by the National Research Foundation of Korea (NRF) grant funded by the Korean government (MSIP) [No. NRF-2020R1A4A2002161].

Supplementary materials

Supplementary material associated with this article can be found, in the online version, at doi:10.1016/j.scriptamat.2020.07.022.

References

[1] D. Meroni, S. Ardizzone, Nanomaterials 8 (2018) 891.
[2] W. Song, G.Y. Guo, S. Huang, L. Yang, L. Yang, Phys. Rev. Appl. 13 (2020) 014052.
[3] M. Abid Derbel, M.M. Turnbull, H. Naïli, W. Rekik, Polyhedron 175 (2020) 114220.
[4] Y. Wen, G. Zhu, Y. Shao, J. Mater. Sci. 55 (2020) 2937–2946.
[5] Z. Liu, S. Dai, Y. Wang, B. Yang, D. Hao, D. Liu, Y. Zhao, L. Fang, Q. Ou, S. Jin, J. Zhao, J. Huang, Adv. Funct. Mater. 30 (2020) 1906335.
[6] H. Xie, S. Zhai, B. Chen, T. Liu, Y. Zhang, M. Ni, Z. Shao, Appl. Energy 260 (2020) 114197.
[7] C. Wilhelm, M. Vafaeezadeh, P. Breuninger, P. Lösch, S. Ernst, S. Antonyuk, W.R. Thiel, Chem. Cat. Chem. 11 (2019) 2304–2312.
[8] W. Jiao, J. He, L. Zhang, Sens. Actuat. B Chem. 309 (2020) 127786.
[9] P. Zhu, S. Li, C. Zhao, Y. Zhang, J. Yu, J. Hazard. Mater. 384 (2020) 121426.
[10] J. Jaiswal, A. Sanger, P. Tiwari, R. Chandra, Sens. Actuat. B Chem. 305 (2020) 127437.
[11] F.I.M. Ali, F. Awwad, Y.E. Greish, A.F.S. Abu-Hani, S.T. Mahmoud, Org. Electron. 76 (2020) 105486.
[12] P. Sukhavattanakul, H. Manuspiya, Carbohydr. Polym. 230 (2020) 115566.
[13] J. Wang, H. Deng, X. Li, C. Yang, Y. Xia, Sens. Actuat. B Chem. 304 (2020) 127317.
[14] C. Zou, J. Hu, Y. Su, Z. Zhou, B. Cai, Z. Tao, T. Huo, N. Hu, Y. Zhang, Sens. Actuat. B Chem. 306 (2020) 127546.
[15] M. Chan-Yeung, M.J. Ashley, S. Grzybowski, Can. Med. Assoc. J. 118 (1978) 1271–1274.
[16] J.W. Gurney, J.M. Unger, C.A. Dorby, J.K. Mitby, S.G. Von Essen, Radiographics 11 (1991) 625–634.
[17] J. Austin, P. Brimblecombe, W.T. Sturges, Air Pollution Science for the 21st Century, Elsevier, 2002.
[18] M. Shao, J. Liu, W. Ding, J. Wang, F. Dong, J. Zhang, J. Mater. Chem. C 8 (2020) 487–494.
[19] D. Gu, X. Wang, W. Liu, X. Li, S. Lin, J. Wang, M.N. Rumyantseva, A.M. Gaskov, S.A. Akbar, Sens. Actuat. B Chem. 305 (2020) 127455.
[20] V.X. Hien, P.T. Hung, J. Han, S. Lee, J.H. Lee, Y.W. Heo, Scr. Mater. 178 (2020) 108–113.
[21] J. Wu, Z. Wu, H. Ding, Y. Wei, W. Huang, X. Yang, Z. Li, L. Qiu, X. Wang, Sens. Actuat. B Chem. 305 (2020) 127445.
[22] K.M. S., A.S. Jose, K. Prajwal, P. Chowdhury, H.C. Barshilia, Sens. Actuat. B Chem. 310 (2020) 127830.
[23] G. Almeida, I. Infante, L. Manna, Science 364 (2019) 833–834 (80-.).
[24] H. Wei, J. Huang, Nat. Commun. 10 (2019) 1–12.
[25] L. Gu, M.M. Tavakoli, D. Zhang, Q. Zhang, A. Waleed, Y. Xiao, K.H. Tsui, Y. Lin, L. Liao, J. Wang, Z. Fan, Adv. Mater. 28 (2016) 9713–9721.
[26] H.S. Kim, S.H. Im, N.G. Park, J. Phys. Chem. C 118 (2014) 5615–5625.
[27] M.A. Stoeckel, M. Gobbi, S. Bonacchi, F. Liscio, L. Ferlauto, E. Orgiu, P. Samorì, Adv. Mater. 29 (2017) 1702469.
[28] Y. Zhuang, W. Yuan, L. Qian, S. Chen, G. Shi, Phys. Chem. Chem. Phys. 19 (2017) 12876–12881.
[29] N. Gupta, O. Nanda, R. Grover, K. Saxena, Org. Electron. 58 (2018) 202–206.
[30] R. Zhu, Y. Zhang, H. Zhong, X. Wang, H. Xiao, Y. Chen, X. Li, J. Phys. Chem. Solids 129 (2019) 270–276.
[31] X. Fu, S. Jiao, N. Dong, G. Lian, T. Zhao, S. Lv, Q. Wang, D. Cui, RSC Adv. 8 (2018) 390–395.
[32] T. Leijtens, G.E. Eperon, N.K. Noel, S.N. Habisreutinger, A. Petrozza, H.J. Snaith, Adv. Energy Mater. 5 (2015) 1500963.
[33] N. Aristidou, I. Sanchez-Molina, T. Chotchuangchutchaval, M. Brown, L. Martinez, T. Rath, S.A. Haque, Angew. Chemie Int. Ed. 54 (2015) 8208–8212.
[34] Y. Zhou, Y. Zhao, Energy Environ. Sci. 12 (2019) 1495–1511.
[35] Y. Chen, X. Zhang, Z. Liu, Z. Zeng, H. Zhao, X. Wang, J. Xu, Microchim. Acta 186 (2019) 1–10.
[36] Y. Ogomi, A. Morita, S. Tsukamoto, T. Saitho, N. Fujikawa, Q. Shen, T. Toyoda, K. Yoshino, S.S. Pandey, T. Ma, S. Hayase, J. Phys. Chem. Lett. 5 (2014) 1004–1011.
[37] H. Chen, M. Zhang, R. Bo, C. Barugkin, J. Zheng, Q. Ma, S. Huang, A.W.Y. Ho-Baillie, K.R. Catchpole, A. Tricoli, Small 14 (2018) 1702571.
[38] H.J. Kim, J.H. Lee, Sens. Actuat. B Chem. 192 (2014) 607–627.
[39] J.K. Wang, K.T. Liao, W.J. Tseng, Ceram. Int. 43 (2017) S541–S546.
[40] H.S. Jeong, M.J. Park, S.H. Kwon, H.J. Joo, S.H. Song, H.I. Kwon, Ceram. Int. 44 (2018) 17283–17289.
[41] B.-Y. Yeh, P.-F. Huang, W.J. Tseng, Nanotechnology 28 (2017) 045501.